RSC Advances

PAPER

View Article Online
View Journal | View Issue

Cite this: *RSC Adv.*, 2023, **13**, 5382

Mechanism of tetraborate and silicate ions on the growth kinetics of microarc oxidation coating on a Ti6Al4V alloy

Dajun Zhai,[a] Tao Qiu,[a] Jun Shen *[a] and Keqin Feng[b]

The growth kinetics mechanism of microarc oxidation (MAO) coatings on Ti6Al4V alloy was studied by designing a binary mixed electrolyte with various SiO_3^{2-} and $B_4O_7^{2-}$ ion ratios *via* scanning electron microscopy, transmission electron microscopy, X-ray diffraction, X-ray photoelectron spectroscopy, and potentiodynamic polarization. When the ratio of $B_4O_7^{2-}$ in the electrolyte is 100%, $B_4O_7^{2-}$ dissolves molten TiO_2 at a high temperature, exposing nano-scale filamentary channels in the barrier layer of MAO coating, resulting in the repeated nucleation of microarc in the same area. When the ratio of SiO_3^{2-} in the binary mixed electrolyte reaches 10%, the amorphous SiO_2 formed by SiO_3^{2-} at high temperatures from discharge blocks discharge channels and induces microarc nucleation in other regions, thus inhabiting the discharge cascade phenomenon. When the ratio of SiO_3^{2-} in the binary mixed electrolyte increases from 15% to 50%, the amounts of molten oxides cover some of the pores formed by the primary microarc discharge, so part of the secondary discharge preferentially generates in the uncovered pores. Finally, the discharge cascade phenomenon occurs. Moreover, the thickness of the MAO coating obtained in the binary mixed electrolyte containing $B_4O_7^{2-}$ and SiO_3^{2-} shows a power function with time.

Received 5th December 2022
Accepted 31st January 2023

DOI: 10.1039/d2ra07755h

rsc.li/rsc-advances

1. Introduction

Titanium alloy is widely used in numerous fields because of its low density, good mechanical property and corrosion resistance.[1] Microarc oxidation (MAO) is a common method used to improve its surface properties. Microarc oxidation ceramic coating has broad applications in national defense, aerospace, mechanical electronics, automobile transportation, petrochemical industry, and biomedical instrument owing to its excellent properties (*e.g.*, high hardness, corrosion resistance, wear resistance, good biocompatibility, and strong metallurgical bonding strength).[2] The functionalization of MAO ceramic coating has become a hot topic in surface modification. Recently, a multi-functional composite coating with antibacterial and biological activities was obtained by doping Ca, P, Sr, Zn, and Ag into MAO coating.[3–6] The wear resistance of the coating was improved by doping graphite, MoS_2, PTFE, Al_2O_3, Si_3N_4, and Si.[3,7–9] The thermal emissivity was regulated by doping V, W, Fe, Co, Ni, and Zr,[10,11] and the catalytic activity was improved by doping Tb, Ag, ZnO, WO_3, FeO, and G-C_3N_4.[12–15]

The MAO mechanism is more complex than anodic oxidation or other surface treatment techniques. It involves complex physical and chemical processes, such as electrochemical reactions, ion motion, material phase transition, and solution ion electrophoretic motion.[16,17] The distribution and energy of microarc during MAO are difficult to control by electrical conditions, leading to uncertain micropore growth structures in ceramic coatings. However, owing to the non-uniformity of the chemical composition and microstructure of the titanium alloy prepared by applying traditional forming methods (such as casting, forging and welding), the physical and electrochemical state of titanium alloy may be uneven, resulting in cascade discharge[17,18] on the titanium alloy surface during the MAO treatment. Moreover, the microarc plasma has micro–nano spatial distribution, micro–millisecond time distribution, and 4000 K high-temperature energy distribution, resulting in unstable microarcs on the material surface.[19] The physical characteristics and temporal and spatial distributions of each microarc evolve with increasing processing time. For example, the size and temperature of each microarc increase spontaneously as the size and porosity of the micropores increase, and even spark discharges in the form of streamers at the end of the MAO treatment damage the coating.[20] The cascade discharge caused by the instantaneous and unstable characteristics of microarc can seriously damage the substrate structure, reduce the mechanical properties and corrosion resistance of the local area of the coating, and make the coating performance

[a]*College of Materials Science and Engineering, Chongqing University, Chongqing 400044, China. E-mail: shenjun@cqu.edu.cn; zhaidajun05@163.com; 15271836649@163.com*

[b]*College of Mechanical Engineering, Sichuan University, Chengdu 610065, China. E-mail: kqfeng@scu.edu.cn*

unstable. This brings significant challenges to the on-demand construction and utilization of MAO coatings with different structures, thereby limiting their applications in material processing.

MAO plasma is mainly affected by electrolyte composition, electrical parameters, and substrate materials. Electrolyte composition plays a crucial role in the MAO coating's growth, microstructure, and properties.[16,20] Guan *et al.*[21] pointed out challenges in the structural and functional design of coating, and the key is the electrolyte's plasma discharge mechanism. Li *et al.*[22] designed a new MAO coating with a micro/nano layered structure by taking advantage of the solubility of tetraborate ions in molten TiO_2. Zou *et al.*[23] proposed optimizing the interface structure and properties of the MAO coating by adjusting the electrolyte composition. Wang *et al.*[24] proposed the MAO treatment in a composite electrolyte to regulate the structure of an oxide coating using an effective interaction between electrolyte components. Li *et al.*[25] found that optimization using silicate and phosphate electrolytes can increase the adhesion and wear resistance of coatings. Shokouhfar *et al.*[26] used phosphate-, silicate-, and borate-based solutions to evaluate the influence of electrolyte composition on the structure, surface morphology, phase composition, and corrosion behavior of the prepared ceramic oxide films (titania). Pavarini *et al.*[27] found that introducing borates can allow the production of compact coating with high hardness, while silicates can increase their thickness and porosity. Both can help overcome the drawbacks of most phosphate- and calcium phosphate-based conventional electrolytes, such as low thermal stability and limited power efficiency. Tsai *et al.*[28] anticipated that studies on cathode current can influence the precise control of microarc. Laveissière *et al.*[29] believed that electrolyte composition influences the chemical composition of the MAO coating because electrolyte compounds, particularly anions, can either be directly integrated into the coating or combined with metal alloys. Therefore, achieving uniform discharge of microarc plasma using blocking, dissolving, and other effects among the components in the mixed electrolyte has significant research potential.

Based on the above investigation, it is assumed that a small amount of molten oxide can be deposited around the discharge pore to inhibit ion transport in this area, thus preventing the nucleation of cascade discharge. A previous study by the authors found that the morphology of molten oxide can be adjusted by adding different anions to the electrolyte.[21,22,26] Therefore, a binary mixed electrolyte containing silicate and tetraborate was designed in this study. The mechanism of SiO_3^{2-} and $B_4O_7^{2-}$ on MAO coating growth was investigated by adjusting the ratio of the anions. The design of the electrolyte is expected to deposit a small amount of SiO_2 around the pores to inhibit cascade discharge and to obtain a coating with uniformly distributed micro–nano discharge pores, which can be applied to the bioactive coating. This study provides a strategic and theoretical basis for exploring microarc plasma regulation and has important research significance.

Table 1 Electrolyte composition

Group	Molarity of $B_4O_7^{2-}$ (mol L^{-1})	Molarity of SiO_3^{2-} (mol L^{-1})
B10	0.1	0
B9Si1	0.09	0.01
B8.5Si1.5	0.085	0.015
B5Si5	0.05	0.05

2. Experiment materials and method

The Ti6Al4V alloy (Baoji Ti Industry Co. Ltd, China) with chemical composition Ti-6.1Al-4.1V-0.3Fe-0.2O-0.015H (wt%), as an anode, was made into samples of size d10 × 5 mm. Pulse power (AN 5005, Wuxi Anasy Electronic Technology Co. Ltd, China) was used for MAO treatment by employing rectangular pulses with a pulse amplitude of 5 A dm^{-2}. The applied frequency and power duty cycle were set to 200 Hz and 10%, respectively. The electrolytes $Na_2B_4O_7 \cdot 10H_2O$ and $Na_2SiO_4 \cdot 9H_2O$ were stirred, and their temperature was kept below 30 °C. The composition of the electrolytes is given in Table 1. Moreover, the coating growth based on the voltage-time response of the MAO process was investigated at 30, 240, 600, 960, and 1800 s.

The MAO coating surface and cross-section morphologies and compositions were observed by employing a scanning electron microscope (SEM, Phenom ProX, Funa Scientific Instruments Co. Ltd, Netherlands) and a transmission electron microscope (TEM, JEM-2100F, JEOL Co. Ltd, Japan). The coating thickness was detected using a coating thickness gauge (DUALSCOPE®MP0, Fischer, Germany). A probe contact surface profiler (Alpha-step IQ, KLA Tencor, USA) with a measurement speed of 50 μm s^{-1} and a scanning frequency of 50 Hz was used to measure a sample of 10 mm in length. The thickness of each sample was measured ten times at different locations. Cu K_α radiation was used at 40 kV and 30 mA over a 2θ range of 10° to 90° with a scan speed of 0.1° s^{-1} to analyze the phase composition of the coating using X-ray diffraction (XRD, AL-2700B, Aolong Ray Instrument Group Co. Ltd, China). The potentiodynamic polarization curves of the MAO-treated samples were carried out in a 3.5 wt% NaCl solution using a CS120 electrochemical measurement system with a scan rate of 0.1 mV s^{-1}, from −0.4 to 0.2 V. Prior to the test, all samples were immersed in the test solution for 4 h to attain stable open circuit potential.

3. Results and discussion

3.1 Voltage-time response of the MAO process

Fig. 1 shows the voltage-time response of the MAO process in the B/Si electrolyte. According to the discharge intensity, the voltage curves are divided into three stages, namely, anodic oxidation (stage I), spark discharge (stage II), and microarc discharge (stage III), which are also adopted in many studies.[21,30,31] In stage I, the anode voltages increase rapidly and linearly with the formation of bubbles but no discharge spark. When the processing time exceeds 7 s, some faintly visible sparks appear on the sample surface. In addition, the voltage

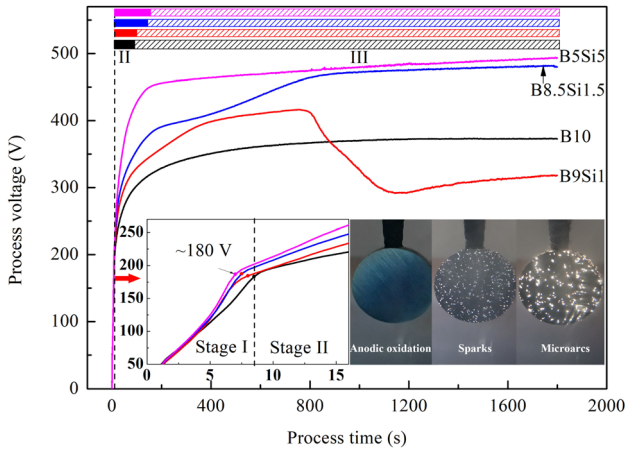

Fig. 1 Voltage-time response during the MAO process in B/Si electrolyte.

growth rate decreases, indicating that the anodized film had broken down. The breakdown voltage of the anodized films on all samples reached ~180 V, indicating that the electrolyte composition insignificantly affects the anodization process. In stage II, the anode voltage increases slowly and nonlinearly, and many white sparks appeared on the sample surface. Comparing the results, it was found that the higher the concentration of SiO_3^{2-} in B/Si electrolyte, the higher the voltage growth rate and the longer the time of stage II, indicating that SiO_3^{2-} inhibits the nucleation of microarc and slows the lateral growth of MAO coatings. In stage III, the voltage growth is further slower than that of the previous stage, which indicates that the rate of secondary microarc discharge is slower than that of primary microarc discharge. However, a steep increase in voltage is observed from 200 to 900 s in the B8.5Si1.5 electrolyte, while the voltage decreases steeply at 800 s in the B9Si1 electrolyte. Moreover, the number of sparks on the B9Si1 samples increases gradually, but the intensity of microarc decreases. The reasons for this are discussed in the following subsection.

3.2 Characteristics of MAO coatings

Fig. 2 shows the surface morphology of the MAO coatings obtained in B/Si electrolyte. After 30 s of treatment, as shown in Fig. 2(a), many submicron pores (~0.5 μm in diameter) and some worm-like channels (~3 × 1 μm in size) are observed on the sample B10 surface. The former pore is formed by the primary spark discharge, which is usually called the primary pore; the latter pore is reported to be formed by the microarc cascade discharge,[17,18] so it is called the cascade pore here. By increasing SiO_3^{2-} concentration in B/Si electrolyte, worm-like cascade pores gradually disappear and more primary pores appear. When treated for 240 s, as shown in Fig. 2(b), amounts of primary pores cover the whole surface of sample B10, and some discharge pores with a diameter of 1–2 μm were observed. These pores, which are larger than the primary pores, are formed by the secondary microarc discharge and are usually called secondary pores. These secondary pores are concentrated on the surface of sample B10, and some of them are connected to form worm-like morphology. The diameter of the secondary pore on the surface of samples B9Si1 and B8.5Si1.5 increases to 2–3 μm, and some molten oxides remain on the surface of the samples, forming a typical crater morphology. This shows that a small amount of SiO_3^{2-} ion can increase the single microarc intensity but inhabits the nucleation of cascade discharge. With the further increase in the concentration of SiO_3^{2-} in the electrolyte, it was observed that a large number of molten oxides accumulated on the surface of sample B5Si5, resulting in a cascade pore with a diameter of 2–5 μm. It can be observed that a high concentration of SiO_3^{2-} in the electrolyte also promotes the cascade discharge.

As the treatment time reached 1800 s, as shown in Fig. 2(c), the number of secondary pores on the surface of sample B10 increases, but the distribution of these pores is still concentrated. The serious cascade of microarcs caused the peeling of some coatings, forming a strip or ring-shaped pore morphology. Many evenly distributed secondary pores and a small amount of residual molten oxide were observed on the surface of sample B9Si1. Based on the above analysis of the voltage-time response, the voltage decreases steeply at stage III in the B9Si1 electrolyte. Therefore, it can be inferred from the voltage curve that the outer deposition layer (formed by the accumulation of molten oxides) on the B9Si1 sample may fall off into the electrolyte. With the further increase in the concentration of SiO_3^{2-} in the electrolyte, it was observed that some amounts of molten oxides accumulated on the surface of samples B8.5Si1.5 and B5Si5, resulting in a cascade pore with a diameter of 5–10 μm. This shows that the higher the concentration of SiO_3^{2-} in the electrolyte, the more serious the discharge cascade phenomenon, the larger the size of the cascade pores formed, and the more residual molten oxides accumulated on the surface of the sample. Moreover, the element content of the MAO coating obtained at 1800 s was detected by EDS mapping, and the results are listed in Table 2. The substrate elements Ti, Al and V and electrolyte elements Si, B and O were detected on the surface of the MAO coating. It was found that the content of electrolyte elements Si and B in the MAO coating on samples B8.5Si1.5 and B5Si5 is higher than that on samples B10 and B9Si1, but the content of substrate elements Ti, Al and V on them is the opposite. Based on the above analysis, it can be observed that the molten oxides on the surfaces of samples B10 and B9Si1 are dissolved by $B_4O_7^{2-}$ (confirmed by some reports[32]), thus exposing the internal structure of the coating. However, the molten oxides on the surfaces of samples B8.5Si1.5 and B5Si5 were not completely dissolved and deposited on the coating surface to form the outer layer. It has been reported that Si forms amorphous SiO_2,[33] co-deposited with molten oxides in MAO coating. Therefore, it can be concluded that the inner layer of the MAO coating contains higher substrate elements than the outer layer, and the electrolyte elements are mainly co-deposited in the outer molten oxide. The above findings provide a theory for the design of biological coatings containing different functional elements on the surface of titanium alloys.

Fig. 3 shows the cross-sectional morphology of the MAO coatings obtained at 1800 s and the EDS spectra of the MAO

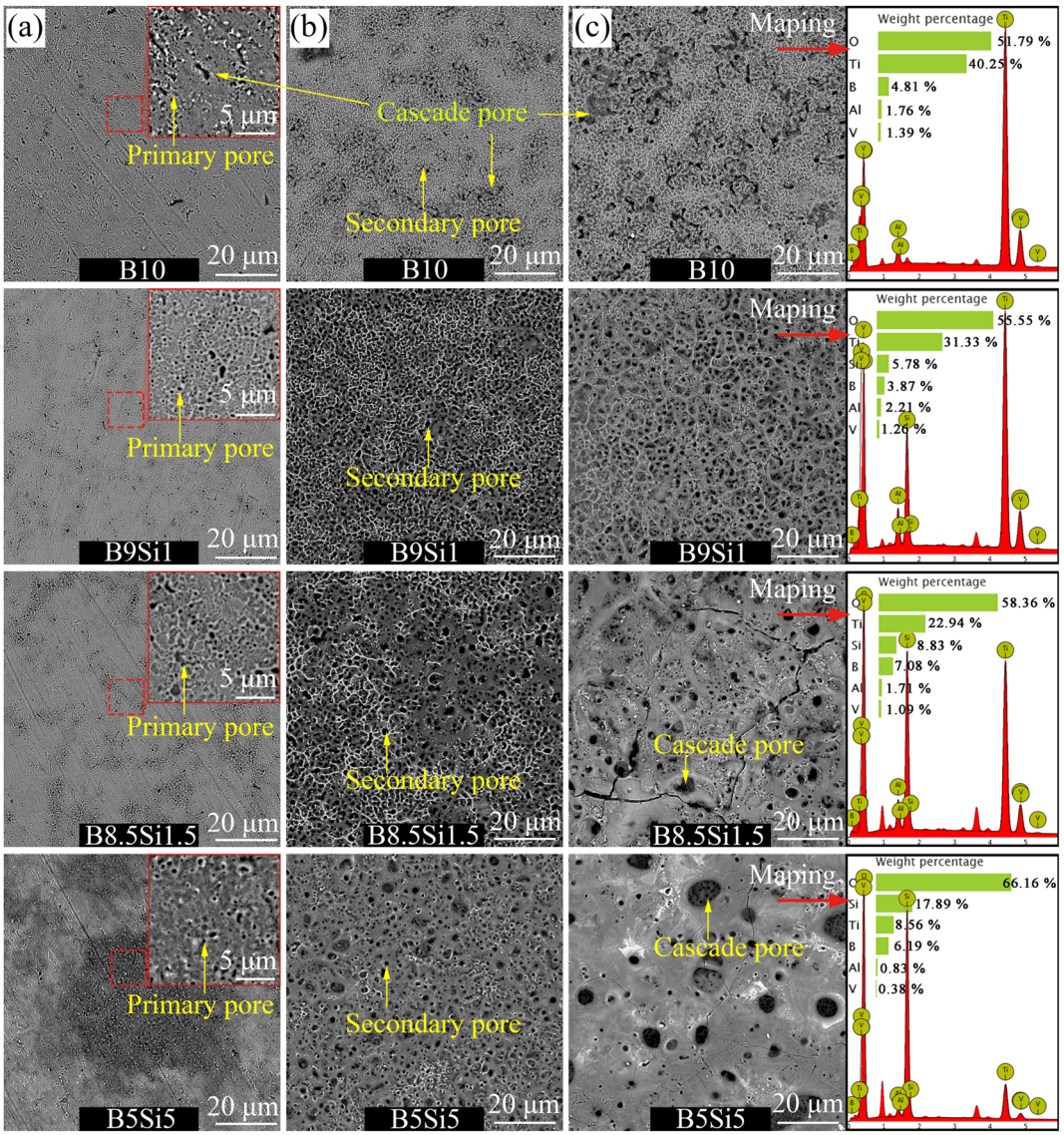

Fig. 2 Surface morphology and EDS mapping results of the MAO coatings obtained at (a) 30 s, (b) 240 s, and (c) 1800 s on samples B10, B9Si1, B8.5Si1.5, and B5Si5.

Table 2 Surface element contents of the MAO coatings obtained at 1800 s

Sample	O (wt%)	Ti (wt%)	B (wt%)	Si (wt%)	Al (wt%)	V (wt%)
B10	51.79	40.25	4.81	0	1.76	1.39
B9Si1	55.55	31.33	3.87	5.78	2.21	1.26
B8.5Si1.5	58.36	22.94	7.08	8.83	1.71	1.09
B5Si5	66.16	8.56	6.19	17.89	0.83	0.38

coating obtained on the B10 sample. As shown in Fig. 3(a), a dense oxide layer with a thickness of ~0.6 μm can be observed at the coating/substrate interface on the B10 sample, which is often referred to as the barrier layer.[34,35] Some pits are observed in this layer from the cascade discharge. Moreover, an inner layer (hereinafter, the primary layer) formed by primary discharge is observed outside the barrier layer in the B10 electrolyte, where some elements B are detected on the primary layer surface by EDS line scanning. It has been reported that B may replace Ti to form inclusions (TiBO3 or B-doped rutile phase) at high temperatures.[32] It can be concluded that element B in the electrolyte can be co-deposited into the primary layer in the coating. As shown in Fig. 3(b), the surface of the primary layer on the B9Si1 sample is relatively flat but its thickness is very thin (~5 μm). The reason is that the outer deposition layer (hereinafter, the secondary layer) on the B9Si1 sample falls off based on the analysis of process voltage and coating surface morphology. As shown in Fig. 3(c), the thickness of the secondary layer on the B8.5Si1.5 sample reaches 30–40 μm. Some large interconnecting holes are observed between the primary and secondary layers. These large holes, called hat-shaped holes, are generated by the cascade of filamentous sparks.[36] With increasing SiO_3^{2-} concentration in B/Si

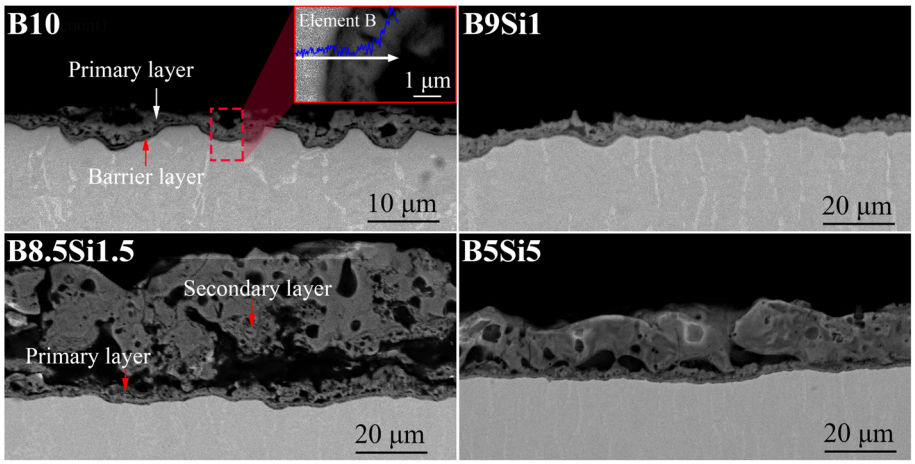

Fig. 3 Cross-sectional morphology of the MAO coatings obtained on the B10, B9Si1, B8.5Si1.5, and B5Si5 samples at 1800 s and EDS spectra of the MAO coating obtained on the B10 sample.

electrolyte, as shown in Fig. 3(d), the thickness of the secondary layer in the coating decreases to ~30 μm, the hat-shaped pore size in the coating decreases, and the density of the secondary layer coating increases. It can be observed that the higher the concentration of $B_4O_7^{2-}$, the larger the hat-shaped hole and the thicker the secondary layer (containing dissolved molten TiO_2), indicating that $B_4O_7^{2-}$ significantly increases the cascade discharge intensity. However, $B_4O_7^{2-}$ reacts with molten TiO_2 to form soluble salts, resulting in a thin coating on the B10 and B9Si1 samples.

The surface roughness variation curves of the MAO coatings in B/Si electrolytes are shown in Fig. 4. The surface roughness of both the B10 and B9Si1 MAO coatings is low and increases slowly as the MAO time increases. This is due to the small size of the filamentary discharge pores and the fact that all the generated molten oxides are dissolved, so their surface roughness is small in all cases. However, the surface roughness of the B8.5Si1.5 and B5Si5 MAO coatings is large and increases as the treatment time increases. The surface roughness of MAO coatings is mainly determined by the accumulation of molten oxides.

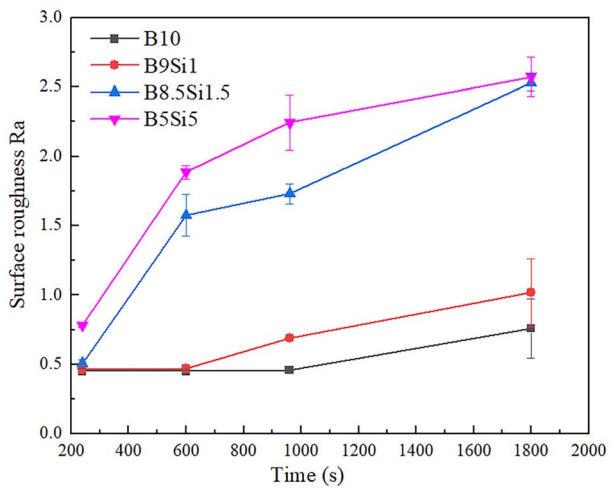

Fig. 4 The surface roughness variation curves of MAO coatings in B/Si mixed electrolytes.

Fig. 5 shows the TEM image and selected area diffraction pattern of the cross-sectional morphology of the MAO coating obtained at 1800 s. As shown in Fig. 4(a), an amorphous layer with a thickness of ~50 nm was observed at the coating/substrate interface, on which there is a thick layer of nanocrystal phase mixed with the amorphous. The diffraction planes of (101), (103), (211), (110), (210), and (200) indicate that the nanocrystals mainly have anatase and rutile phases. TEM image of the barrier layer of the MAO coating obtained on the B10 sample at 1800 s and its high magnification image are shown in Fig. 5(b). An amorphous layer of 100–500 nm thickness is observed at the coating/substrate interface; many nanochannels are found in the barrier layer of the coating on the B10 sample. These channels could have formed owing to discharge or gas escape from molten TiO_2. We infer that the anions in electrolyte reach the barrier layer through these nanochannels, reducing the coating breakdown voltage for filamentous discharge.

The XPS result of the MAO coating obtained in the B5Si5 electrolyte at 1800 s is depicted in Fig. 6. The characteristic peaks of the MAO coating include O 1s, Ti 2p, C 1s, B 1s, Si 2p, and Al 2p (Fig. 6(a)). The C 1s peak at 285.4 eV in the spectrum may be caused by the surface contamination of the coating and requires calibration.[21] The Ti 2p spectra exhibit a doublet with Ti $2p_{3/2}$ and Ti $2p_{1/2}$ peaks at 458.9 and 464.6 eV, respectively (Fig. 6(b)), indicating that Ti exists as TiO_2 in MAO coating.[33] The Al 2p spectra exhibit peaks at 74.23 eV and 74.93 eV (Fig. 6(c)), indicating that Al exists as Al_2O_3 in MAO coating.[21] For the B 1s spectra (Fig. 6(d)), the deconvoluted peak at 192.7 eV binding energy is assigned to B 1s in B_2O_3.[21] The characteristic peak of Si 2p spectra at 102.7 eV can be identified as Si 2p in SiO_2 (Fig. 6(e)).[33] The O 1s spectrum has four peaks (Fig. 6(f)). The peak with a bond energy of 532.6 eV is SiO_2, while

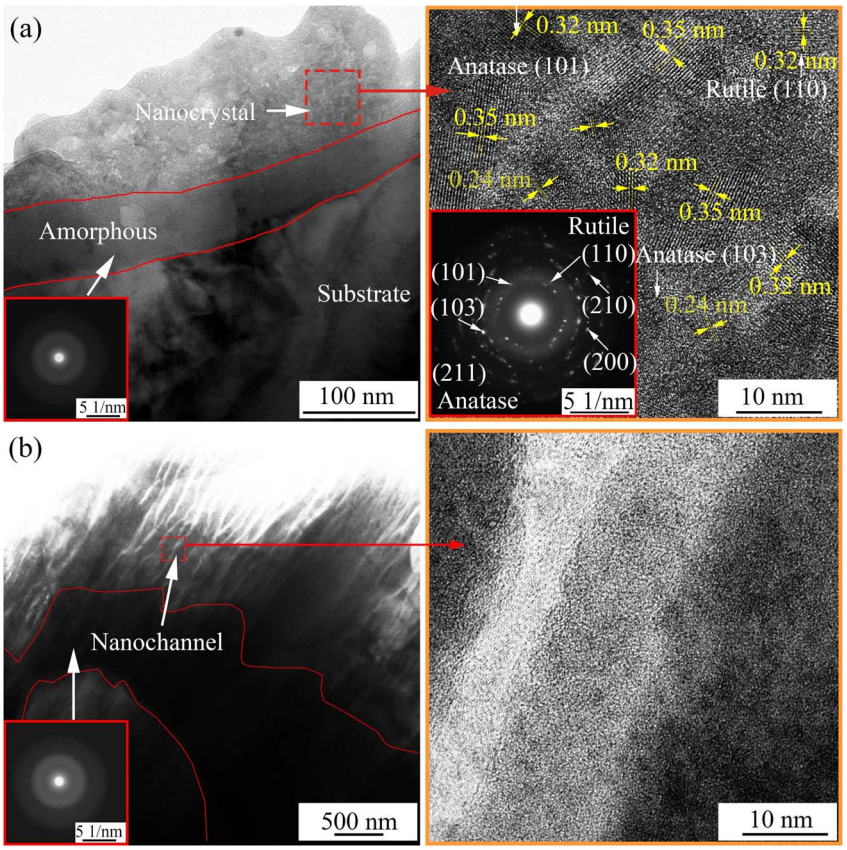

Fig. 5 TEM image and selected area diffraction pattern of the cross-sectional morphology of MAO coating obtained at 1800 s on samples (a) B5Si5 and (b) B10.

the peak with a bond energy of 530.2 eV is TiO_2.[21,33] The peak at 532.1 eV corresponds to B_2O_3, while the peak at 531.1 eV corresponds to Al_2O_3.[21,37] The XRD patterns show that the MAO coatings obtained in B/Si electrolytes mainly comprise rutile and anatase TiO_2 (Fig. 7). No characteristic peaks of SiO_2 and B_2O_3 are detected in the XRD pattern, suggesting that these contents in the MAO coating are small or exist in the amorphous phase. A broad peak exists between 15° and 30° in the pattern of the B5Si5 coating, while the broad peaks at the same position are not obvious in the patterns of the other groups. This is probably because B_2O_3 is easily soluble in water,[21] so the diffraction intensity of the broad peak is determined by water-insoluble SiO_2. The B5Si5 coating with the highest Si content contains more amorphous SiO_2, resulting in a more pronounced broad peak. The adiabatic method[38] quantitatively analyzes the phase content, and the results are shown in Table 3. Compared to the anatase phase, the contents of the rutile phase in the coating are significantly higher because of the transition from the former to the latter at high temperatures during plasma discharge. As SiO_3^{2-} increases, the anatase phase in the coating increases, while the rutile phase first increases and then decreases, reaching the maximum for the B8.5Si1.5 sample. Based on the above analysis, it can be observed that the intensity of the cascade discharge increases as the $B_4O_7^{2-}$ concentration increases in the B/Si electrolyte, resulting in more rutile at higher temperatures. However, the low rutile phase in the B10 and B9Si1 samples results from the dissolution of molten TiO_2 by $B_4O_7^{2-}$.

3.3 Electrochemical responses of the MAO coatings

Fig. 8 shows the potentiodynamic polarization curves of the MAO coatings obtained at 1800 s. The Tafel constants (β_a and β_c), corrosion potential (E_{corr}), and corrosion current density (i_{corr}) are derived from the data using Tafel extrapolation. The polarization resistance (R_p), calculated using the Stern–Geary equation,[39] is presented in Table 4. The results show that the MAO coating on the B10 sample has higher polarization resistance than those on the B5Si5, B8.5Si1.5, and B9Si1 samples. When small traces of SiO_3^{2-} are added to the B/Si electrolyte, the polarization resistance (*e.g.*, B9Si1 sample) decreases significantly. The coating formed by cascade discharge has a thicker barrier layer and better corrosion resistance. However, as the SiO_3^{2-} concentration increases in the B5Si5 and B8.5Si1.5 electrolytes, the coating thickness decreases, but polarization resistance increases slightly. This is because amorphous SiO_2 formed by SiO_3^{2-} at high temperatures co-deposits with molten oxides, blocking the discharge channels and increasing the coating density.

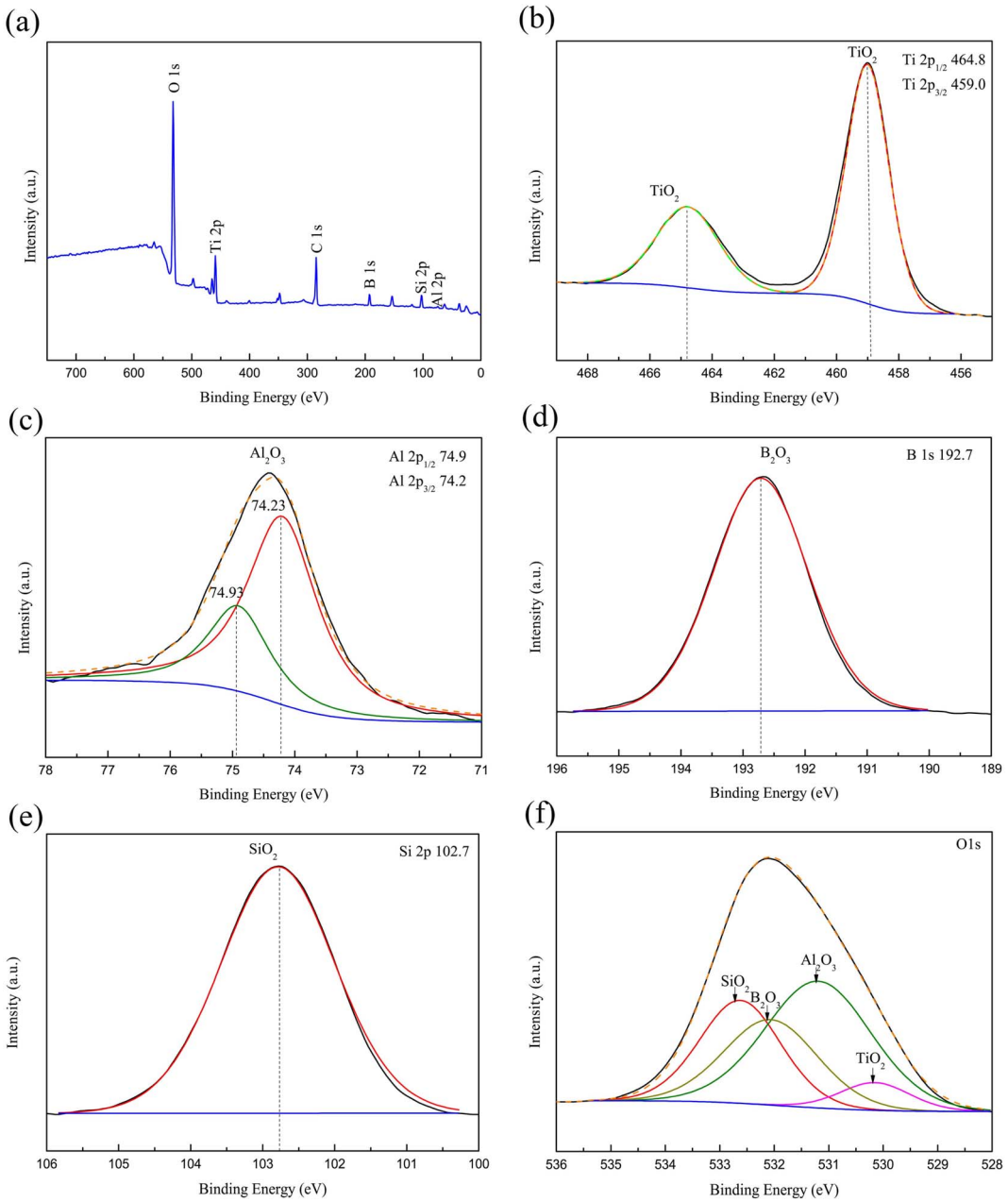

Fig. 6 The XPS result of the MAO coating obtained in the B5Si5 electrolyte at 1800 s: (a) wide-survey spectrum, (b) Ti 2p spectrum, (c) Al 2p spectrum, (d) B 1s spectrum, (e) Si 2p and (f) O 1s spectrum of MAO coating obtained at 1800 s in the B5Si5 electrolyte.

3.4 Mechanism of $B_4O_7^{2-}$ and SiO_3^{2-} on MAO coating growth

Fig. 9 shows the thickness variation of the MAO coatings obtained in the B/Si electrolyte. Most reports indicate that the MAO coating grows linearly in an electrolyte that cannot dissolve molten TiO_2.[25,40] This is because one stage of microarc discharge represents the lateral growth of a layer in the coating, during which the average strength of the microarcs is approximately equal,[41] that is, the coating growth rate is a constant during each stage. The higher the microarc strength, the more molten TiO_2 produces, and the faster the lateral growth of the MAO coating. However, it is reported that B_2O_3 formed from $B_4O_7^{2-}$ at high temperatures can dissolve molten TiO_2 at high temperatures formed by discharge,[21,22,32] resulting in slower lateral growth of the MAO coating. This process can be described by the following reaction:[21,22]

$$Ti \rightarrow Ti^{4+} + 4e^{-}, \quad (1)$$

$$Ti^{4+} + 2O^{2-} \rightarrow TiO_2, \quad (2)$$

$$B_4O_7^{2-} \rightarrow B_2O_3 + O^{2-}, \quad (3)$$

$$pTiO_2 + qB_2O_3 \rightarrow (pTiO_2 \cdot qB_2O_3), \quad (4)$$

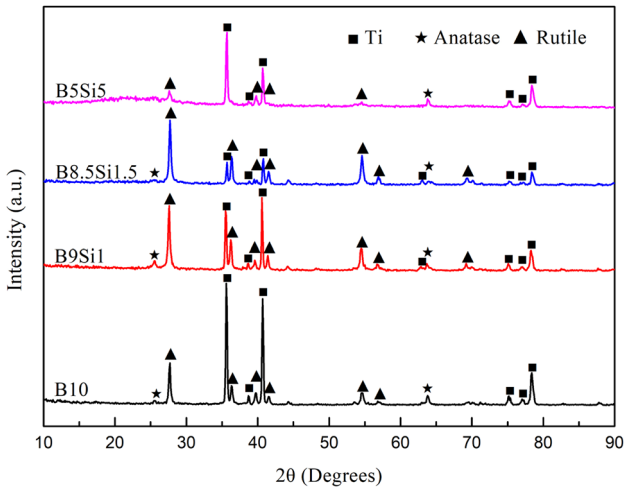

Fig. 7 XRD patterns of the MAO coatings obtained at 1800 s in B/Si electrolytes.

Table 3 Mass variation of the phases during the MAO process

	Mass variation (wt%)		
Group	Rutile	Anatase	Ti & amorphous
B10	17.26	0.98	81.76
B9Si1	31.25	2.54	66.21
B8.5Si1.5	54.77	2.59	42.64
B5Si5	17.74	6.11	76.15

where $(pTiO_2 \cdot qB_2O_3)$ represents a mixture of TiO_2 and B_2O_3 that can be dissolved in electrolyte.[21,22] Therefore, the MAO coating grows nonlinearly in tetraborate electrolytes. After fitting, it was found that the thickness of the coating obtained in different B/Si electrolytes increased in a power function with time, which can be described by the following equation:

Table 4 Potentiodynamic polarization data of the MAO coatings obtained at 1800 s in B/Si electrolyte

Sample	β_a (mV)	β_c (mV)	i_{corr} (μA cm^{-2})	E_{corr} (mV)	R_p (kΩ cm^2)
B10	1952.2	1919.1	10.51	−0.091612	39.975
B9Si1	1355.9	1630.8	18.24	−0.159	17.62
B8.5Si1.5	1688.2	2457.8	31.35	−0.27316	13.864
B5Si5	1373.8	1784	16.66	−0.14423	20.363

$$d = at^b, \quad (5)$$

where b is a constant related to the dissolution rate of molten TiO_2 and a is a constant related to the composition of the electrolyte. The dissolution rate is related to the high temperature produced by the microarc discharge. The high temperature produced by a single discharge is constant in a stage because the intensity of a single microarc is approximately equal at that stage.[41] Therefore, b is a constant in each stage. The thickness of the MAO coatings obtained in stage III was fitted based on eqn (5), and the response function for the different samples is obtained as follows:

$$d_{B10} = 1.32t^{0.24}, \quad (6)$$

$$d_{B9Si1} = 0.89t^{0.37}, \quad (7)$$

$$d_{B8.5Si1.5} = 0.31t^{0.59}, \quad (8)$$

$$d_{B5Si5} = 0.25t^{0.61} \quad (9)$$

According to the above analysis, the sudden decrease in coating thickness at 960 s in the B9Si1 electrolyte is probably due to coating exfoliation. Most studies ignore coating exfoliation when fitting the growth of coating thickness. The value of a increases gradually as the $B_4O_7^{2-}$ concentration increases in the electrolyte, indicating an increasing growth rate of the

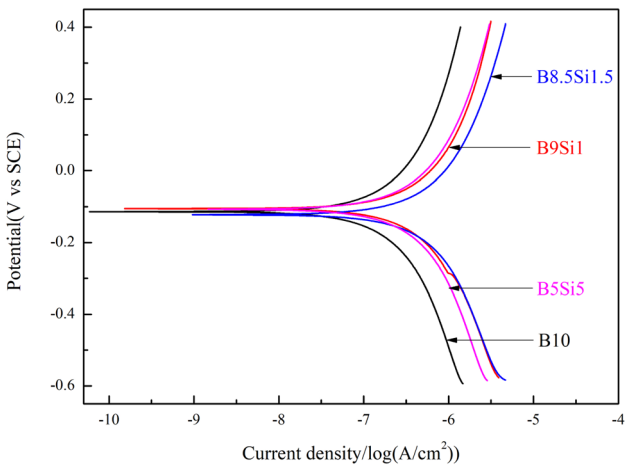

Fig. 8 Potentiodynamic polarization curves of the MAO coatings obtained at 1800 s.

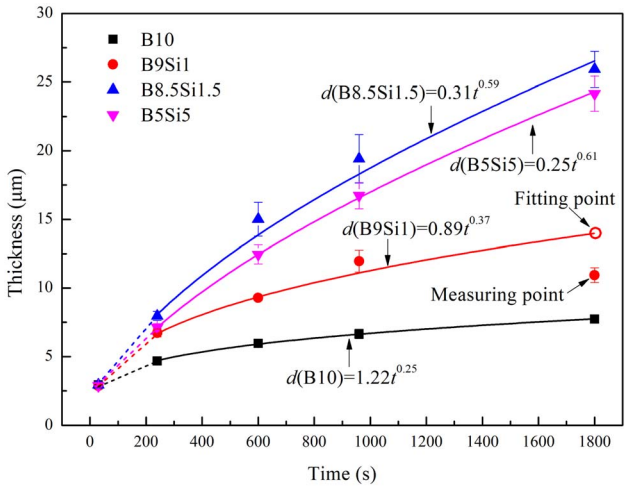

Fig. 9 Thickness variation of the MAO coatings obtained in B/Si electrolyte.

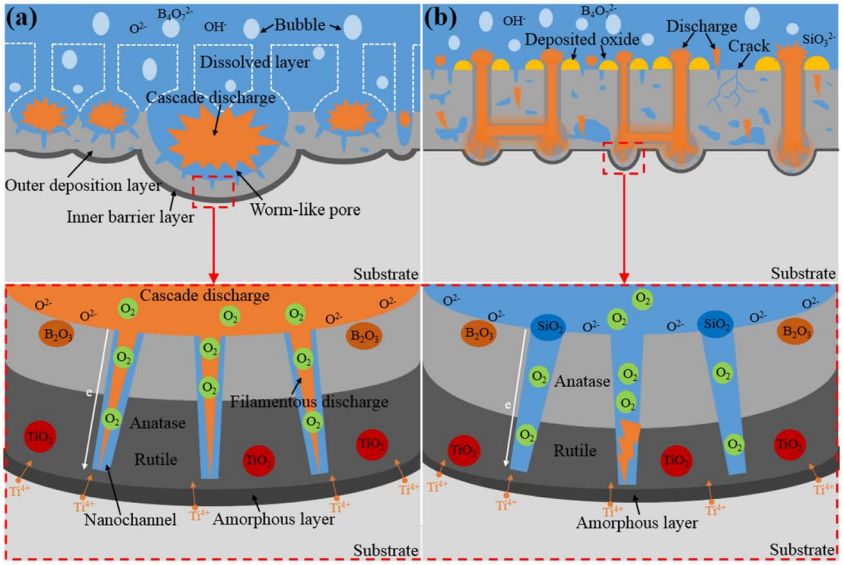

Fig. 10 Schematic of the coating evolution during the MAO process in (a) B10 and (b) B/Si electrolyte.

coating thickness (containing dissolved oxides). This inference agrees with the results of the above analysis. However, *b* shows a decreasing trend as the $B_4O_7^{2-}$ concentration increases in the electrolyte, indicating that the higher the SiO_3^{2-} concentration, the smaller the dissolution rate of molten TiO_2 and the larger the linear growth of the coating thickness. This inference agrees with that obtained by other researchers in an insoluble electrolyte.[25]

Based on the above results, we conclude that the B/Si electrolyte with high SiO_3^{2-} concentrations reduces the number of microarcs but increases their intensity over time. A schematic structure of the MAO coatings prepared in the B/Si electrolyte is presented in Fig. 10 to reveal the mechanism of SiO_3^{2-} and $B_4O_7^{2-}$ on MAO coating growth.

Fig. 10(a) presents the structure of the MAO coating obtained in the B10 electrolyte. Studies have shown that B_2O_3 can dissolve the molten TiO_2.[21,22,32] The larger the concentration of $B_4O_7^{2-}$ in the B/Si electrolyte, the more B_2O_3 formed at a high temperature, the stronger their dissolution on the coating, and the slower their growth rate. In addition, the oxides around the discharge channel are completely dissolved, thereby exposing the channels produced by gas escape or microarc discharge in the dense barrier layer (see Fig. 5(b)). Then, the ions in the electrolyte can easily reach the barrier layer through these channels. The dielectric strength of the coating is reduced,[21] and the microarcs are easy to repeat around the channel (*i.e.*, cascade discharge phenomenon) by increasing the number of microarcs. Because most microarcs are cascaded in the local area of the sample, forming a few large pits (*i.e.*, cascade pores), $B_4O_7^{2-}$ has been mistaken for inhibiting the increase in microarc numbers.

Fig. 10(b) depicts the structure of the MAO coating obtained in B/Si electrolyte (such as B9Si1, B1.5Si8.5, and B5Si5). The amorphous SiO_2 formed by SiO_3^{2-} at high temperatures from discharge is insoluble in alkaline electrolyte and is deposited on the sample, thus promoting the growth of the coating.[25] However, the co-deposited SiO_2 blocks discharge channels and gas pores, which makes repeated discharge more difficult in the same region, thus initiating microarcs in other regions. However, the intensity of the new microarc is greater than that of the previous one. Therefore, SiO_3^{2-} results in fewer microarcs and a slow growth of coating thickness. For the same treatment time, the higher the concentration of SiO_3^{2-}, the thinner the barrier layer of the coating (see Fig. 3 and 5) because SiO_3^{2-} inhibits cascade discharge without influencing the intensity growth for signal microarc.

4. Conclusion

The mechanism of SiO_3^{2-} and $B_4O_7^{2-}$ on MAO coating growth was investigated by adjusting the ratio of anions in the binary mixed electrolyte. When the ratio of $B_4O_7^{2-}$ in the electrolyte is 100%, the $B_4O_7^{2-}$ dissolve molten TiO_2 at high temperature, thereby exposing nano-scale filamentary channels in the barrier layer of MAO coating, resulting in repeated nucleation of microarc in the same area. When the ratio of SiO_3^{2-} in the binary mixed electrolyte reaches 10%, the amorphous SiO_2 formed by SiO_3^{2-} at high temperatures from discharge blocks discharge channels and induces microarc nucleation in other regions, thus inhabiting the discharge cascade phenomenon. When the ratio of SiO_3^{2-} in the binary mixed electrolyte increases from 15% to 50%, the amounts of molten oxides cover some of the pores formed by the primary microarc discharge, so part of the secondary discharge preferentially generates in the uncovered pores. Finally, the discharge cascade phenomenon occurs. Moreover, the thickness of the MAO coating obtained in a binary mixed electrolyte containing $B_4O_7^{2-}$ and SiO_3^{2-} shows a power function with time. $B_4O_7^{2-}$ increased the number of discharges (mostly in cascade form), while SiO_3^{2-} reduced the number of discharges but enhanced the intensity of a single microarc at each stage.

Conflicts of interest

There are no conflicts of interest to declare.

Acknowledgements

This research is funded by China Postdoctoral Science Foundation (Grant No. 2021M700569) and Chongqing Postdoctoral Science Foundation (Grant No. cstc2021jcyj-bshX0087).

References

1 X. Yang, W. J. Ma, W. P. Gu, *et al.*, Multi-scale microstructure high-strength titanium alloy lattice structure manufactured via selective laser melting, *RSC Adv.*, 2021, **11**, 22734–22743.
2 Z. Yang, Z. Zhang, Y. Chen, *et al.*, Controllable in situ fabrication of self-lubricating nanocomposite coating for light alloys, *Scr. Mater.*, 2022, **211**, 114493.
3 Z. Wu, J. Luo, J. Zhang, *et al.*, Silver-Releasing Micro-/Nanoporous Coating on Additively Manufactured Macroporous Ti-Ta-Nb-Zr Scaffolds with High Osseointegration and Antibacterial Properties, *Coatings*, 2021, **11**, 716.
4 J. Yao, Y. Wang, G. Wu, *et al.*, Growth characteristics and properties of micro-arc oxidation coating on SLM-produced TC4 alloy for biomedical applications, *Appl. Surf. Sci.*, 2019, **479**, 727–737.
5 H. Xing, R. Li, Y. Wei, *et al.*, Improved Osteogenesis of Selective-Laser-Melted Titanium Alloy by Coating Strontium-Doped Phosphate with High- Efficiency Air-Plasma Treatment, *Front. Bioeng. Biotechnol.*, 2020, **8**, 367.
6 F. Wu, R. Xu, X. Yu, *et al.*, Enhanced Biocompatibility and Antibacterial Activity of Selective Laser Melting Titanium with Zinc-Doped Micro-Nano Topography, *J. Nanomater.*, 2019, **2019**, 5432040.
7 X. Yan, C. Chen, R. Bolot, *et al.*, Improvement of tribological performance by micro-arc oxidation treatment on selective laser melting Ti6Al4V alloy, *Mater. Res. Express*, 2019, **6**, 096509.
8 X. Sun, S. Tong, S. Yang, *et al.*, The Effects of Graphene on the Biocompatibility of a 3D-Printed Porous Titanium Alloy, *Coatings*, 2021, **11**, 1509.
9 Y. Guo, L. Xu, J. Luan, *et al.*, Effect of carbon nanotubes additive on tribocorrosion performance of micro-arc oxidized coatings on Ti6Al4V alloy, *Surf. Interfaces*, 2022, **28**, 101626.
10 G. Liao, Q. Li, W. Zhao, *et al.*, In situ construction of novel silver nanoparticle decorated polymeric spheres as highly active and stable catalysts for reduction of methylene blue dye, *Appl. Catal., A*, 2018, **549**, 102–111.
11 M. Adigamova, I. Lukiyanchuk, I. Tkachenko, *et al.*, Fe-, Ni-containing ceramic-like PEO coatings on titanium and aluminum: Comparative analysis of the formation features, composition and ferromagnetic properties, *Mater. Chem. Phys.*, 2022, **275**, 125231.
12 S. Stojadinović, N. Tadić, N. Radić, *et al.*, Effect of Tb^{3+} doping on the photocatalytic activity of TiO_2 coatings formed by plasma electrolytic oxidation of titanium, *Surf. Coat. Technol.*, 2018, **337**, 279–289.
13 W. Tao, M. Wang, R. Ali, *et al.*, Multi-layered porous hierarchical TiO_2/g-C_3N_4 hybrid coating for enhanced visible light photocatalysis, *Appl. Surf. Sci.*, 2019, **495**, 143435.
14 H. Qin, L. Chen, X. Yu, *et al.*, Preparation and photocatalytic performance of ZnO/WO_3/TiO_2 composite coatings formed by plasma electrolytic oxidation, *J. Mater. Sci.: Mater. Electron.*, 2018, **29**, 2060–2071.
15 M. S. Vasilyeva, V. S. Rudnev, A. A. Zvereva, *et al.*, FeO_x, SiO_2, TiO_2/Ti composites prepared using plasma electrolytic oxidation as photo-Fenton-like catalysts for phenol degradation, *J. Photochem. Photobiol., A*, 2018, **356**, 38–45.
16 S. Sikdar, P. Menezes, R. Maccione, *et al.*, Plasma Electrolytic Oxidation (PEO) Process-Processing, Properties, and Applications, *Nanomaterials*, 2021, **11**, 1375.
17 S. Troughton, A. Nomine, J. Dean, *et al.*, Effect of individual discharge cascades on the microstructure of plasma electrolytic oxidation coatings, *Appl. Surf. Sci.*, 2016, **389**, 260–269.
18 A. Nomine, S. Troughton, A. Nomine, *et al.*, High speed video evidence for localised discharge cascades during plasma electrolytic oxidation, *Surf. Coat. Technol.*, 2015, **269**, 125–130.
19 R. Hussein, X. Nie and D. Northwood, A spectroscopic and microstructural study of oxide coatings produced on a Ti-6Al-4V alloy by plasma electrolytic oxidation, *Mater. Chem. Phys.*, 2012, **134**, 484–492.
20 F. Simchen, M. Sieber, A. Kopp, *et al.*, Introduction to Plasma Electrolytic Oxidation-An Overview of the Process and Applications, *Coatings*, 2020, **10**, 628.
21 S. Guan, M. Qi, Y. Li, *et al.*, Morphology evolution of the porous coatings on Ti–xAl alloys by Al adding into Ti during micro-arc oxidation in $Na_2B_4O_7$ electrolyte, *Surf. Coat. Technol.*, 2020, **395**, 125948.
22 Y. Li, W. Wang, H. Liu, *et al.*, Formation and in vitro/in vivo performance of "cortex-like" micro/nano-structured TiO_2 coatings on titanium by micro-arc oxidation, *Mater. Sci. Eng., C*, 2018, **87**, 90–103.
23 Y. Zou, V. Wang, D. Wei, *et al.*, In-situ SEM analysis of brittle plasma electrolytic oxidation coating bonded to plastic aluminum substrate: Microstructure and fracturebehaviors, *Mater. Charact.*, 2019, **156**, 109851.
24 Y. Wang, P. Zhang, Y. Du, *et al.*, Correlations between the Growth Mechanism and Corrosion Resistance of Plasma Electrolytic Oxidation Coatings on AZ31B Magnesium Alloy, *Int. J. Electrochem. Sci.*, 2019, **14**, 11465–11479.
25 Q. Li, W. Yang, C. Liu, *et al.*, Correlations between the growth mechanism and properties of micro-arc oxidation coatings on titanium alloy: effects of electrolytes, *Surf. Coat. Technol.*, 2017, **316**, 162–167.
26 M. Shokouhfar, C. Dehghanian, M. Montazeri, *et al.*, Preparation of ceramic coating on Ti substrate by plasma electrolytic oxidation in different electrolytes and evaluation of its corrosion resistance: Part II, *Appl. Surf. Sci.*, 2012, **258**, 2416–2423.

27 M. Pavarini, M. Moscatelli, G. Candiani, *et al.*, Influence of frequency and duty cycle on the properties of antibacterial borate-based PEO coatings on titanium for bone-contact applications, *Appl. Surf. Sci.*, 2021, **567**, 150811.
28 D. Tsai and C. Chou, Influences of Growth Species and Inclusions on the Current–Voltage Behavior of Plasma Electrolytic Oxidation: A Review, *Coatings*, 2021, **11**, 270.
29 M. Laveissière, H. Cerda, J. Roche, *et al.*, In-depth study of the influence of electrolyte composition on coatings prepared by plasma electrolytic oxidation of TA6V alloy, *Surf. Coat. Technol.*, 2019, **361**, 50–62.
30 G. Mortazavi, J. Jiang and E. Meletis, Investigation of the plasma electrolytic oxidation mechanism of titanium, *Appl. Surf. Sci.*, 2019, **488**, 370–382.
31 X. Zhang, G. Cai, Y. Lv, *et al.*, Growth mechanism of titania on titanium substrate during the early stage of plasma electrolytic oxidation, *Surf. Coat. Technol.*, 2020, **400**, 126202.
32 V. Rudnev, M. Vasilyeva, N. Kondrikov, *et al.*, Plasma-electrolytic formation, composition and catalytic activity of manganese oxide containing structures on titanium, *Appl. Surf. Sci.*, 2005, **252**, 1211–1220.
33 J. Han, Y. Cheng, W. Tu, *et al.*, The black and white coatings on Ti-6Al-4V alloy or pure titanium by plasma electrolytic oxidation in concentrated silicate electrolyte, *Appl. Surf. Sci.*, 2017, **428**, 684–697.
34 S. Franz, H. Arab, G. Chiarello, *et al.*, Single-Step Preparation of Large Area TiO_2 Photoelectrodes for Water Splitting, *Adv. Energy Mater.*, 2020, **10**, 2000652.
35 W. Cui, L. Jin and L. Zhou, Surface characteristics and electrochemical corrosion behavior of a pre-anodized microarc oxidation coating on titanium alloy, *Mater. Sci. Eng., C*, 2013, **33**, 3775–3779.
36 D. Wang, X. Liu, Y. Wu, *et al.*, Evolution process of the plasma electrolytic oxidation (PEO) coating formed on aluminum in an alkaline sodium hexametaphosphate ($(NaPO_3)_{(6)}$) electrolyte, *J. Alloys Compd.*, 2019, **798**, 129–143.
37 Y. L. Cheng, Z. G. Xue, Q. Wang, *et al.*, New findings on properties of plasma electrolytic oxidation coatings from study of an Al-Cu-Li alloy, *Electrochim. Acta*, 2013, **107**, 358–378.
38 S. Popovic, Quantitative Phase Analysis by X-ray Diffraction-Doping Methods and Applications, *Crystals*, 2020, **10**, 27.
39 M. Nadimi and C. Dehghanian, Incorporation of ZnO–ZrO_2 nanoparticles into TiO_2 coatings obtained by PEO on Ti-6Al-4V substrate and evaluation of its corrosion behavior, microstructural and antibacterial effects exposed to SBF solution, *Ceram. Int.*, 2021, **47**, 33413–33425.
40 O. Terleeva, Y. Sharkeev, A. Slonova, *et al.*, Effect of microplasma modes and electrolyte composition on micro-arc oxidation coatings on titanium for medical applications, *Surf. Coat. Technol.*, 2010, **205**, 1723–1729.
41 T. Clyne and S. Troughton, A review of recent work on discharge characteristics during plasma electrolytic oxidation of various metals, *Int. Mater. Rev.*, 2019, **64**, 127–162.